PHYSICAL REVIEW D **94,** 014020 (2016)

Simulating collisions of thick nuclei in the color glass condensate framework

Daniil Gelfand,[*] Andreas Ipp,[†] and David Müller[‡]
Institut für Theoretische Physik, Technische Universität Wien,
Wiedner Hauptstraße 8-10, A-1040 Vienna, Austria
(Received 1 June 2016; published 19 July 2016)

We present our work on the simulation of the early stages of heavy-ion collisions with finite longitudinal thickness in the laboratory frame in $3+1$ dimensions. In particular we study the effects of nuclear thickness on the production of a glasma state in the McLerran-Venugopalan model within the color glass condensate framework. A finite thickness enables us to describe nuclei at lower energies, but forces us to abandon boost invariance. As a consequence, random classical color sources within the nuclei have to be included in the simulation, which is achieved by using the colored particle-in-cell method. We show that the description in the laboratory frame agrees with boost-invariant approaches as a limiting case. Furthermore we investigate collisions beyond boost invariance, in particular the pressure anisotropy in the glasma.

DOI: 10.1103/PhysRevD.94.014020

I. INTRODUCTION

Heavy ion collisions allow us to study strongly interacting matter in a deconfined phase, the quark gluon plasma. In search for a critical point in the QCD phase diagram, experiments cover a wide range of collision energies, from very high energies at RHIC and LHC, down to lower energies in the Beam Energy Scan program of RHIC [1] and at future programs at GSI FAIR and JINR NICA. The early times of heavy ion collisions can be appropriately described in the color glass condensate (CGC) framework [2,3].

The CGC framework models ultrarelativistic, highly Lorentz-contracted nuclei in terms of an effective classical field theory. Hard partons are described as color charges, which act as sources for the soft partons in terms of classical non-Abelian gauge fields due to gluon saturation. The distribution of the color charges of very large nuclei is given by the McLerran-Venugopalan (MV) model [4,5]. More recent sophisticated models such as IP-Glasma base the color charge distribution on fits to deep-inelastic scattering data [6,7]. As a result of the collision the glasma is produced [8], which can be studied by numerically solving the Yang-Mills equations.

A common simplification is to assume infinitely thin incoming nuclei, which leads to a single collision point in time and consequently to boost invariance. This reduces the system to effectively $2+1$ dimensions [9–11]. In this formulation the gauge fields are rapidity independent by assumption. It is possible to introduce rapidity dependence by including boost-invariance breaking fluctuations on top of boost-invariant background fields [12–14]. However, the initial conditions and evolution of the background fields are still formulated in a boost-invariant way. Simulations of the early stages of heavy-ion collisions using the CGC framework and real-time lattice gauge theory have been highly successful in describing particle multiplicities [15] and the azimuthal anisotropy [16,17]. Studies of somewhat later time intervals involving isotropization and thermalization of the glasma have been undertaken using classical-statistical lattice gauge theory with [18] and without fermions [19–22], hard loop approximation [23–27] as well as kinetic theory [28–31]. Within the CGC framework, there has also been progress in finding analytical solutions for the gauge fields in the forward light cone using expansions in small τ [32–34]. Because of the infinitesimal thickness of nuclei in all the boost-invariant approaches, the evolution of the color sources can be solved analytically.

Nontrivial evolution of color sources in the form of charged particles can be simulated using the colored particle-in-cell method (CPIC) method. It combines classical field dynamics described by real-time non-Abelian lattice gauge theory [35] with classical colored particle dynamics based on Wong's equations [36]. It is a non-Abelian generalization of the particle-in-cell (PIC) method for the simulation of Abelian plasmas [37]. CPIC has been successfully applied to hard-thermal-loop simulations [38,39], the investigation of plasma instabilities [40,41] and to jet energy loss [42] in the quark-gluon plasma. Apart from pioneering work [43–45] for very small transversal lattices this approach has not been used yet to investigate the collision itself.

In this paper, we simulate the collision of two nuclei with finite thickness in the laboratory frame in $3+1$ dimensions in the CGC framework. A finite nuclear thickness enables us to describe nuclei at lower energies. Without a well-defined collision point, we have to drop the assumption of boost invariance for the fields in the forward light cone. As a consequence of an extended collision, we cannot describe the evolution of the color sources analytically and we are forced to include the color charges as dynamical degrees of freedom in the simulation as they traverse the evolving

[*]gelfand@hep.itp.tuwien.ac.at
[†]ipp@hep.itp.tuwien.ac.at
[‡]david.mueller@tuwien.ac.at

overlap region of the two nuclei. In studying lower collision energies, we are probing the limits of applicability of the CGC framework, which becomes an accurate effective description of QCD only at infinitely high energies. The goal of this work is to show that a description in the laboratory frame using CPIC is viable and can reproduce well-known results of boost-invariant classical Yang-Mills simulations in the limit of small longitudinal thickness of the nuclei. For simplicity we restrict ourselves to collisions in the MV model, which describes ultrarelativistic nuclear matter infinitely extended in the transversal directions, and to the gauge group SU(2). We do not take into account other possible effects that might come into play if the CGC picture is applied to lower energies, but simply approach this region as a first step by varying the thickness of the incoming nuclei.

This paper is organized as follows: In Sec. II we describe the CPIC method for heavy-ion collisions. We discuss the equations of motion for the fields and color charges and initial conditions in the laboratory frame. In Sec. III we present our numerical results for collisions in the MV model with finite thickness. We investigate the structure of the fields in the forward light cone created during the collision and compare them to the initial conditions used in boost-invariant simulations. We recover the usual result of pressure anisotropy and investigate the energy conservation in the system.

II. COLORED PARTICLE-IN-CELL METHOD FOR HEAVY-ION COLLISIONS

The model of a heavy-ion collision which we implement in this work is that of two sheets of color fields and charges, each occupying a two-dimensional plane, colliding with each other at the speed of light in the laboratory frame. The sheets modeling Lorentz contracted nuclei as depicted in Fig. 1 have a finite extent in the longitudinal direction in which they propagate and a largely random transversal color structure. On the other hand, in our setup the longitudinal color structure is assumed to be coherent, spreading a given color configuration over the complete thickness of a nucleus. Each of the sheets consists of two contributions, a charge distribution and its corresponding classical fields. The charge distributions are chosen according to the McLerran-Venugopalan model and are not directly participating in the collision dynamics while being tied to the light cone. In our CPIC approach we model these charges as classical particles with a non-Abelian color charge. Following the core assumptions of the CGC framework, the charges generate classical gluon fields, which travel alongside them in the sheet and are responsible for the creation of matter during and after the collision. The dynamics of these fields are consistently described by Yang-Mills equations without any approximations.

The CPIC method simulates the evolution of colored point charges in continuous phase space coupled to non-Abelian gauge fields on a discrete lattice. In each simulation step, the equations of motion for particles and fields are solved alternately. Currents for the field equations are obtained by interpolating the motion of charges to the lattice, while interpolating the discretized fields back to the continuous particle positions gives rise to forces and parallel transport. The simulation volume is modeled as a three-dimensional grid with $N_L \cdot N_T^2$ cells, where N_L and N_T are the number of cells in the longitudinal and transversal directions respectively with spatial lattice spacing a_s and time step a_t. In each cell we define the electric fields $E_{x,i}$, the gauge links $U_{x,i}$, and the charge and current densities ρ_x and $j_{x,i}$, where x denotes the lattice site of the cell and $i \in \{1, 2, 3\}$ is a vector index. The box is periodic in the transversal directions and fixed boundary conditions are used for the longitudinal direction.

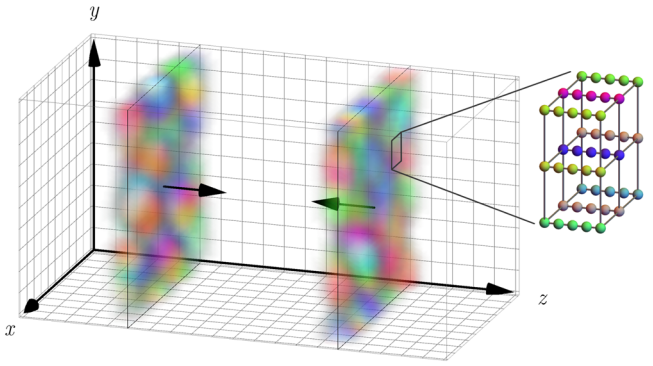

FIG. 1. Schematic overview of a heavy-ion collision modeled with CPIC in the laboratory frame. The random color charge densities of the nuclei are modeled by placing color charge carrying particles (here depicted as small spheres) into each cell along the longitudinal direction. These particles move continuously in the longitudinal direction, but are fixed to the grid points in the transversal plane.

The initial conditions for the fields are generated from the charge densities ρ_1 and ρ_2 of the two nuclei. This step is described in Sec. II C. The exact form of $\rho_{(1,2)}$ depends on the model used to describe the nuclei. We choose the longitudinal separation of the nuclei such that the fields do not overlap in the beginning. The color charge densities $\rho_{(1,2)}$ are then used to sample the particle charges. We place N_p particles in each cell and apply the charge refinement algorithm from Sec. II D to get a smooth distribution of color charges among the particles. The fields and particles are then evolved via the lattice equations of motion (see Sec. II A) and the nearest-grid-point interpolation method (see Sec. II B). Consequently, the Gauss constraint is fulfilled throughout the simulation of the system. Similar to most collision simulations in the color glass condensate framework we do not take the backreaction from the fields onto the particles into account (apart from parallel transport of the charges), i.e. the particles' velocity is held constant at the speed of light. As a consequence the particles act as a

reservoir of energy for the fields and total energy is not conserved. The maximum simulation time is limited by the longitudinal length of the simulation box, since the nuclei are continuously moving in the longitudinal direction and will reach the end of the box after some time. The color charge density $\rho^a(x)$ is treated as a random variable following a probability functional $W[\rho]$ given by the MV model. Observables are recorded during the simulation and then averaged using a number of different initial charge densities $\rho_{(1,2)}$ according to $W[\rho]$.

A. Field equations of motion

In this section we review the standard lattice Yang-Mills equations of motion. We start by discretizing the continuum Yang-Mills action

$$S = \int d^4x \left[-\frac{1}{2}\mathrm{tr}(F_{\mu\nu}F^{\mu\nu}) + 2\mathrm{tr}(j_\mu A^\mu) \right], \quad (2.1)$$

with current density j_μ, gauge field $A_{x,\mu} \equiv A_\mu(x) = A^a_{x,\mu}t^a$, and field strength tensor $F_{\mu\nu} = \partial_\mu A_\nu - \partial_\nu A_\mu - ig[A_\mu, A_\nu]$, on a hypercubic lattice taking advantage of the lattice gauge formalism in Minkowski space. The gauge links $U_{x,i}$ and $U_{x,0}$ at the lattice site x are defined by

$$U_{x,i} = \exp(iga_s A_{x,i}), \quad (2.2)$$

$$U_{x,0} = \exp(iga_t A_{x,0}), \quad (2.3)$$

with the temporal and spatial lattice spacings a_t and a_s. We also define $U_{x,-\mu} \equiv U^\dagger_{x-\mu,\mu}$ and the plaquette variables

$$U_{x,ij} = U_{x,i}U_{x+i,j}U^\dagger_{x+j,i}U^\dagger_{x,j} \simeq \exp\left(iga_s^2 F_{x,ij}\right), \quad (2.4)$$

$$U_{x,0i} = U_{x,0}U_{x+0,i}U^\dagger_{x+i,0}U^\dagger_{x,i} \simeq \exp\left(iga_s a_t F_{x,0i}\right), \quad (2.5)$$

where $F_{x,ij}$ and $F_{x,0i}$ are components of the non-Abelian field-strength tensor. The continuum action can then be approximated as

$$S \simeq S_{\mathrm{YM}} + S_J, \quad (2.6)$$

with the Yang-Mills part

$$S_{\mathrm{YM}} = \frac{a_s}{g^2 a_t}\sum_x \left(\sum_{i=1}^{3} \mathrm{tr}[U_{x,0i} + U^\dagger_{x,0i}] - \frac{1}{2}\left(\frac{a_t}{a_s}\right)^2 \sum_{i=1}^{3}\sum_{j=1}^{3} \mathrm{tr}[U_{x,ij} + U^\dagger_{x,ij}] \right) + C, \quad (2.7)$$

and the source terms

$$S_J = 2a_s^3 a_t \sum_x \left(\mathrm{tr}[\rho_x A_{x,0}] - \sum_{i=1}^{3} \mathrm{tr}[j_{x,i}A_{x,i}] \right), \quad (2.8)$$

where C is an irrelevant constant. By varying the discretized action with respect to the gauge fields $A_{x,\mu}$ and employing the temporal gauge $U_{x,0} = \mathbf{1}$, which corresponds to $A_0 = 0$, we obtain the discretized equations of motion. For our numerical approach we choose the electric field $E_{x,i} \equiv F^{i0}$ and the spatial gauge links $U_{x,i}$ as our degrees of freedom. The equations can be solved numerically using a leap-frog scheme, where the electric fields $E_{x,i}$ and charge density ρ_x are evaluated at whole time steps $t_n = na_t$, while the gauge links $U_{x,i}$ and current density $j_{x,i}$ are evaluated at half time steps $t_{n+\frac{1}{2}} = (n+\frac{1}{2})a_t$. The discretized equations then read

$$U_{x,i}\left(t + \frac{a_t}{2}\right) = \exp\left(-ia_t g a_s E_{x,i}(t)\right) U_{x,i}\left(t - \frac{a_t}{2}\right), \quad (2.9)$$

$$E^a_{x,i}(t + a_t) = E^a_{x,i}(t) + \frac{a_t}{g a_s^3}\sum_{j\neq i} 2\mathrm{Im}\ \mathrm{tr}\left[t^a U_{x,ij}\left(t + \frac{a_t}{2}\right) + t^a U_{x,i-j}\left(t + \frac{a_t}{2}\right)\right] - a_t j^a_{x,i}\left(t + \frac{a_t}{2}\right). \quad (2.10)$$

Since the Gauss constraint

$$\sum_{i=1}^{3} \frac{E_{x,i}(t) - U^\dagger_{x-i,i}(t - \frac{a_t}{2})E_{x-i,i}(t)U_{x-i,i}(t - \frac{a_t}{2})}{a_s} = \rho_x(t) \quad (2.11)$$

must be preserved at every time step, the charge density ρ_x and the current density $j_{x,i}$ must obey the covariant continuity equation, i.e.

$$\frac{\rho_x(t) - \rho_x(t - a_t)}{a_t} + \sum_{i=1}^{3} \frac{j_{x,i}(t - \frac{a_t}{2}) - U^\dagger_{x-i,i}(t - \frac{a_t}{2})j_{x-i,i}(t - \frac{a_t}{2})U_{x-i,i}(t - \frac{a_t}{2})}{a_s} = 0. \quad (2.12)$$

B. Particle equations of motion and interpolation

In the CGC framework hard partons are described by classical color sources in terms of the charge density ρ_x. Within our simulations we sample ρ_x by a number of pointlike particles carrying color charge. The interpolation step reconstructs the charge density from the particle charges and continuous positions. In the transverse plane of the heavy ion, we place one particle per cell in order to match the resolution of the grid. As we will see later, multiple particles per cell in the propagating direction are needed for better resolution of the longitudinal profile. While the colored particles move through the grid, they induce color currents j_x^a, which are used to evolve the gauge fields via the lattice equations of motion (2.9) and (2.10). A main requirement is that the Gauss constraint (2.11) must be satisfied at all times. This can be accomplished by making sure that the currents generated by the particle movement satisfy the covariant continuity equation (2.12). This is the main idea behind charge-conserving methods, which are commonly used in Abelian PIC simulations [46].

One of the assumptions of the color glass condensate framework is that the nuclei involved in the collision can be thought of as recoilless sources moving at the speed of light. The charges of the nuclei pass through each other without loss of energy or change of momentum, i.e. the particle trajectories are fixed. The longitudinal particle positions $z(t)$ are simply updated with

$$z(t+a_t) = z(t) + v a_t, \tag{2.13}$$

with the velocity $v = \pm 1$. This renders the interpolation problem one dimensional in the longitudinal direction. Using this simplification the continuity equation (2.12) reads

$$\frac{\rho_x(t) - \rho_x(t-a_t)}{a_t} + \frac{j_x(t-\frac{a_t}{2}) - U^\dagger_{x-e_z}(t-\frac{a_t}{2}) j_{x-e_z}(t-\frac{a_t}{2}) U_{x-e_x}(t-\frac{a_t}{2})}{a_s} = 0, \tag{2.14}$$

where we choose $i = z$ as the longitudinal direction and drop the direction indices.

In the simulation, we also need to interpolate the continuous particle positions to the fixed lattice points of the charge density $\rho_x(t)$. In this work, we implement a simple interpolation method called the nearest-grid-point (NGP) method [39]. In the NGP method a particle charge $Q(t)$ at position $x(t)$ is fully mapped to the closest lattice point n. The charge density contribution at this point from one particle is then given by

$$\rho_n(t) = \frac{Q(t)}{a_s^3}. \tag{2.15}$$

As the charge moves through the grid, the charge density only changes when the particle crosses the boundary in the middle of a cell such that its nearest-grid-point changes. These boundaries can be formally defined as the ones separating two cells on a lattice, which is shifted by half a lattice spacing (Wigner-Seitz lattice), with lattice points now marking the center and not the edges of each cell. A current is only induced at such a boundary crossing. Evaluating the one-dimensional continuity equation (2.14) at $x = n$ and at $x = n+1$ and requiring that the only nonzero current is $j_n(t-\frac{a_t}{2})$, we find for a right-moving particle that moves from position n to $n+1$ from time $t - a_t$ to t the following current and updated charge:

$$j_n\left(t - \frac{a_t}{2}\right) = \frac{a_s}{a_t}\frac{Q(t-a_t)}{a_s^3}, \tag{2.16}$$

$$Q(t) = U_n^\dagger\left(t - \frac{a_t}{2}\right) Q(t-a_t) U_n\left(t - \frac{a_t}{2}\right). \tag{2.17}$$

For the case of a left-moving particle from position n to $n-1$ we get

$$j_{n-1}\left(t - \frac{a_t}{2}\right) = -\frac{a_s}{a_t}\frac{Q(t-a_t)}{a_s^3}, \tag{2.18}$$

$$Q(t) = U_{n-1}\left(t - \frac{a_t}{2}\right) Q(t-a_t) U_{n-1}^\dagger\left(t - \frac{a_t}{2}\right). \tag{2.19}$$

Equations (2.17) and (2.19) take care of the parallel transport of the charges.

The current generated by the NGP scheme can give rise to a lot of numerical noise due to peaklike currents being induced only at certain time steps. However, we can circumvent this problem by initializing multiple particles per cell and by employing charge refinement procedures (see Sec. II D). These improvements allow us to simulate sufficiently accurate currents on the grid. Another way to address this issue is to use more sophisticated interpolation schemes such as the cloud-in-cell (CIC) interpolation, which is standard for Abelian PIC simulations and also has been developed for the CPIC method [40].

C. Initial conditions

As a model of a single nucleus, we want to construct a propagating solution with given color charge $\hat{\rho}^a(x_T)$ (not to be confused with ρ_x, the charge density in three dimensions) in the transverse plane as given by the MV model

with $x_T = (x, y)$ denoting the transverse coordinates. The boost-invariant case assumes that the nucleus is infinitely Lorentz contracted in the longitudinal direction and therefore described by a color current,

$$J^{a\mu} = \delta(z - t)\hat{\rho}^a(x_T)s^\mu, \tag{2.20}$$

with $s^\mu \equiv (1, 0, 0, 1)^\mu$ for a random transverse color charge configuration $\hat{\rho}^a(x_T)$ that travels at the speed of light in the positive z-direction. The restriction we release is the requirement of an infinitely thin nucleus, by spreading the color charge along the longitudinal direction. It is possible to find a corresponding consistent field configuration such that charge and fields both propagate together at the speed of light.

It is easiest to set up the solution in Lorenz gauge $\partial_\mu A^{a\mu} = 0$. We use the following ansatz for the four-current $J^{a\mu} = (\rho^a, j_i^a)$ and vector potential $A^{a\mu}$:

$$J^{a\mu} = f(z - t)\hat{\rho}^a(x_T)s^\mu, \tag{2.21}$$

$$A^{a\mu} = f(z - t)\hat{\varphi}^a(x_T)s^\mu. \tag{2.22}$$

The envelope $f(z - t)$ is arbitrary, and we will choose a Gaussian profile

$$f(z - t) = \frac{1}{\sqrt{2\pi}\sigma} e^{-\frac{(z-t)^2}{2\sigma^2}}, \tag{2.23}$$

with a given width σ, which is proportional to the thickness of the nucleus in the laboratory frame.[1] Plugging the ansatz into the non-Abelian Maxwell equations

$$D_\mu^{ab} F^{b\mu\nu} = J^{a\nu}, \tag{2.24}$$

nonlinear terms vanish due to $s^\mu s_\mu = 0$ and the time dependence drops out because of $s^\mu \partial_\mu f(z - t) = 0$. As a consequence one is left with the Poisson equation

$$-\Delta_T A^{a\nu} \equiv -\left(\frac{\partial^2}{\partial x^2} + \frac{\partial^2}{\partial y^2}\right) A^{a\nu} = J^{a\nu}, \tag{2.25}$$

which is solved in Fourier space for each color component separately and formally denoted using the inverse Laplace operator $\Delta_T^{-1} = (\nabla_T^2)^{-1}$ by

$$\hat{\varphi}^a(x_T) = -\frac{\hat{\rho}^a(x_T)}{\nabla_T^2}. \tag{2.26}$$

The corresponding electric field is then given by

$$E^a_{i=1,2} = f(z - t)\partial_i \hat{\varphi}^a(x_T), \qquad E^a_3 = 0. \tag{2.27}$$

In Lorenz gauge the chromoelectric fields are purely transverse while the gauge fields retain only their temporal and longitudinal components. All fields are nonzero exclusively in the space-time region close to the light cone, where $J^{a\mu}$ is nonvanishing. In order to switch to temporal gauge we apply a gauge transformation to the gauge fields via

$$A'^a_\mu t^a = V\left(A^a_\mu t^a + \frac{i}{g}\partial_\mu\right)V^\dagger, \tag{2.28}$$

such that $A'^a_0(x) = 0$ is fulfilled at all times. Consequently, V must satisfy the equation

$$\frac{\partial}{\partial t} V^\dagger = igA^a_0 t^a V^\dagger. \tag{2.29}$$

Since the gauge field configurations (2.22) commute at different times, the solution to this equation does not require a time-ordered exponential, but is simply given by

$$V^\dagger(t, x, y, z) = \exp\left(ig\hat{\varphi}^a(x, y)t^a F(t, z)\right) \tag{2.30}$$

with $F(t, z) \equiv \int_{-\infty}^{t} f(z - t')dt'$. Using this gauge transformation, the fields in the temporal axial gauge are given by

$$A'^a_{\mu=1,2} t^a = \frac{i}{g} V(\partial_\mu V^\dagger), \qquad A'^a_{\mu=0,3} t^a = 0. \tag{2.31}$$

The current has to be transformed properly into the temporal axial gauge $J'^a_\mu t^a = V(J^a_\mu t^a)V^\dagger$ as well. The corresponding electric field can be calculated from $E^a_i \equiv -\partial^0 A^{ai}$. We make two important observations at this point. In contrast to the situation in Lorenz gauge, the gauge fields are now purely transversal. Additionally, they are now defined not only on the nuclear sheet close to the light cone as before, but also in the spatial region behind each nucleus, forming a trace of constant gauge fields (see Fig. 2). Although these fields are pure gauge configurations, which can be gauge transformed to vacuum and thus do not carry any energy, their emergence forces us to choose fixed boundary conditions in the longitudinal direction.

The Wilson line (2.30) required for the transformation to temporal gauge is completely analogous to the lightlike

[1] In the boost-invariant case it is common to write the expressions $J^{a\mu}$ and $A^{a\mu}$ a bit differently using light-cone coordinates $x^\pm = \frac{1}{\sqrt{2}}(t \pm z)$. One would then write Eq. (2.20) as $J^{a\mu} = \delta(x^-)\hat{\rho}^a(x_T)\bar{s}^\mu$, where $\bar{s}^\mu = \frac{1}{\sqrt{2}}(1, 0, 0, 1)^\mu$ is the unit vector in the $+$ direction. Applying this to nuclei with finite thickness we would have $J^{a\mu} = \bar{f}(x^-)\hat{\rho}^a(x_T)\bar{s}^\mu$ and $A^{a\mu} = \bar{f}(x^-)\hat{\varphi}^a(x_T)\bar{s}^\mu$, where $\bar{f}(x^-)$ is a Gaussian profile with thickness parameter $\bar{\sigma}$. Our convention differs from this by introducing the thickness parameter σ in the laboratory frame coordinates instead of the light-cone coordinate frame. The different conventions for the widths σ and $\bar{\sigma}$ are geometrically related by $\sqrt{2}\bar{\sigma} = \sigma$. In the end it does not matter which convention one uses, but one should be aware that a finite width in the light-cone frame differs from the width in the laboratory frame by a factor of $\sqrt{2}$.

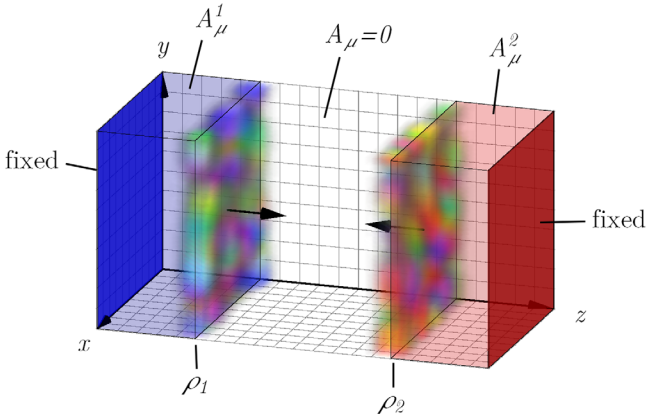

FIG. 2. Schematic overview of the initial conditions in temporal gauge before the collision. The color charge densities $\rho_{(1,2)}$ of the colliding nuclei are depicted as colorful clouds. The gauge field A_μ in the center region of the box is exponentially close to zero. Behind each nucleus the fields asymptotically approach the pure gauge configurations $A^{(1,2)}_\mu$ depicted as blue and red transparent regions. At the longitudinal boundaries of the simulation box the gauge fields are fixed to the static pure gauge configurations.

Wilson lines used in the boost-invariant formulation [2,3]. If we consider $\hat{\rho}^a(x_T)$ as a random variable, the ansatz (2.21) and (2.22) leads to uncorrelated fields in the transversal direction, but correlation over the longitudinal extent of the nucleus. A more general ansatz, which is beyond the scope of the current work, would also allow for fluctuations in the longitudinal direction [47] making a time-ordered exponential in Eq. (2.30) necessary.

Furthermore, we introduce infrared (IR) and ultraviolet (UV) regulators for the solution of the Poisson equation (2.26). This is done by solving in momentum space:

$$\hat{\varphi}^a(k_T) = \begin{cases} \frac{\hat{\rho}^a(k_T)}{|k_T|^2+m^2}, & |k_T| \le \Lambda, \\ 0, & |k_T| > \Lambda, \end{cases} \tag{2.32}$$

where the parameters m and Λ control the IR and UV regulation and $\hat{\varphi}^a(k_T)$, $\hat{\rho}^a(k_T)$ are the Fourier components of $\hat{\varphi}^a(x_T)$ and $\hat{\rho}^a(x_T)$ respectively. The IR regulator m in the expression for $\hat{\varphi}^a$ introduces a finite correlation length on the order of m^{-1} in the transversal directions. The inclusion of the IR regulator and the UV cutoff does not violate the field equations of motion or the Gauss constraint, since it can be absorbed into a redefined charge density

$$\hat{\rho}'^a(k_T) = \frac{|k_T|^2}{|k_T|^2+m^2}\Theta(\Lambda - |k_T|)\hat{\rho}^a(k_T), \tag{2.33}$$

which satisfies the unmodified Poisson equation in momentum space

$$\hat{\varphi}^a(k_T) = \frac{\hat{\rho}'^a(k_T)}{|k_T|^2}. \tag{2.34}$$

Regulating the infrared modes with $m > 0$ also enforces global color neutrality, i.e.

$$\hat{\rho}'^a(k_T = 0) = 0. \tag{2.35}$$

On the lattice we initialize the transversal gauge links at $t_0 - \frac{a_t}{2}$ and $t_0 + \frac{a_t}{2}$ via

$$U_{x,i}\left(t_0 \pm \frac{a_t}{2}\right) = V\left(t_0 \pm \frac{a_t}{2}, x\right) \times V^\dagger\left(t_0 \pm \frac{a_t}{2}, x+i\right), \; i \in \{1,2\}, \tag{2.36}$$

and the longitudinal gauge links are set to the unit element. The initial electric fields $E_{x,i}(t_0)$ are computed from the gauge link update (2.9). We then evaluate the Gauss constraint (2.11) to obtain the correct three-dimensional color charge density $\rho_x(t_0)$, which is sampled by a number of particles. One point charge per transverse grid cell is sufficient to reproduce a given charge density in a transverse plane. The longitudinal structure requires a higher resolution: In order to obtain a smooth current with the NGP algorithm, the charge is distributed among $N_p = a_s/a_t$ particles per cell, which are placed with equal spacing along the longitudinal direction such that at each time step exactly one particle crosses a Wigner-Seitz cell boundary. It is not sufficient to divide the total charge within a cell to the particles equally. The sublattice distribution of the charges has to be optimized with the charge refinement algorithm described in the next section.

D. Charge refinement

Up to this point, we have only specified the total charge in a cell, but not how the charge is distributed within the cell. A constant charge distribution within each cell as seen in Fig. 3 on the left results in a "jittery" color current distribution on the grid over time. This also impacts the evolution of the fields and in particular leads to spurious longitudinal fields in the direction of propagation.[2] In order

[2]To see why this is the case consider the equation of motion of the longitudinal chromoelectric field. This argument can already be made with the Abelian equation $\dot{E}_L = (\vec{\nabla} \times \vec{B})_L - j_L$. The electric and magnetic fields of a single nucleus moving at the speed of light are purely transverse, there are no longitudinal components. Consequently, the longitudinal current must satisfy $j_L = (\vec{\nabla} \times \vec{B})_L$ at all times at each point in space. Any deviation from this produces longitudinal chromoelectric fields, which in turn affect the future time evolution of the other fields. In our simulations the spatial shape and time behavior of the interpolated current depend on the sublattice distribution of particle charges. A smooth distribution of the charges is better at preserving the transversal field structure.

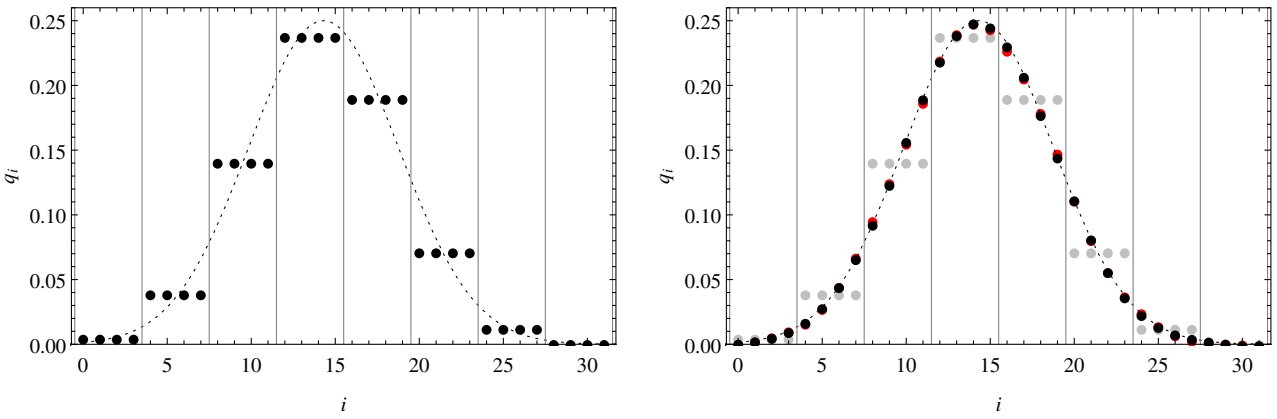

FIG. 3. Example of charge refinement: the small charge q_i is plotted as a function of the position i for $N_\mathrm{p} = 4$ small charges per cell. In the left plot, an initial total charge per Wigner-Seitz cell (separated by the gray vertical lines and given in this example by the integral of the dashed line per cell) is equally distributed among four small charges per cell. After applying the charge refinement algorithm (right plot), the total charge per Wigner-Seitz cell is exactly the same as in the left plot, but it approximates the continuous charge distribution (dashed line) significantly better. Red dots indicate the result for constant discrete second derivative, Eq. (2.41), while black dots show the result for constant discrete fourth derivative within a cell, Eq. (2.43).

to avoid this, the shape of the charge distribution should be as smooth as possible as seen in Fig. 3 on the right.

For the NGP algorithm, we have to satisfy that the sum of all small charges within a Wigner-Seitz cell equals its given total charge Q_j. In order to distribute the total cell charge Q_j to N_p small charges q_i with $N_\mathrm{p} j \le i < N_\mathrm{p}(j+1)$ within the cell, we can initialize them according to

$$q_i = \frac{Q_j}{N_\mathrm{p}}, \quad \text{for } N_\mathrm{p} j \le i < N_\mathrm{p}(j+1). \tag{2.37}$$

We then apply an iterative procedure that ensures that the total charge within a cell is not altered. At each iteration step, two randomly chosen neighboring charges q_i and q_{i+1} (with $i+1$ not a multiple of N_p) are assigned new values q_i' and q_{i+1}' according to

$$q_i' = q_i - \Delta q, \tag{2.38}$$

$$q_{i+1}' = q_{i+1} + \Delta q. \tag{2.39}$$

This ensures for arbitrary Δq that the total charge within the cell is not modified. If one demands that the discrete second derivative is constant within a cell, which is equivalent to demanding that the discrete first derivatives of adjacent points form an arithmetic series

$$\frac{q_{i+1}' - q_i'}{a_s} = \frac{1}{2}\left[\frac{q_{i+2} - q_{i+1}}{a_s} + \frac{q_i - q_{i-1}}{a_s}\right], \tag{2.40}$$

then we find

$$\Delta q = \frac{q_{i+2} - 3q_{i+1} + 3q_i - q_{i-1}}{4}. \tag{2.41}$$

Applying Eqs. (2.38) and (2.39) with (2.41) repeatedly to all points leads to a convergent solution that is continuous and piecewise linear in the first derivative. The algorithm cannot be applied directly to the border of two cells (i.e. $i = N_\mathrm{p} j - 1$), so these points have to be left out.

One can also demand that the discrete third derivatives form an arithmetic series:

$$\frac{q_{i+2} - 3q_{i+1}' + 3q_i' - q_{i-1}}{a_s^3} = \frac{1}{2}\left[\frac{q_{i+3} - 3q_{i+2} + 3q_{i+1} - q_i}{a_s^3} + \frac{q_{i+1} - 3q_i + 3q_{i-1} - q_{i-2}}{a_s^3}\right]. \tag{2.42}$$

On the left-hand side, we use that q_{i+2} and q_{i-1} remain untransformed. The result is

$$\Delta q = \frac{-q_{i+3} + 5q_{i+2} - 10q_{i+1} + 10q_i - 5q_{i-1} + q_{i-2}}{12}. \tag{2.43}$$

Convergence is fastest if the results are first iterated according to condition (2.41) and then according to (2.43). An example of this procedure is shown in Fig. 3.

E. Simulation cycle

For comprehensiveness we summarize the individual steps in our simulations. First we generate initial conditions using the methods described in the last two sections. This

includes generating random charge distributions according to the MV model, solving the two-dimensional Poisson equation and initializing the chromoelectric fields and gauge links in the temporal gauge. The Gauss constraint is then used to obtain the charge density on the grid, which is sampled by a number of colored particles. The distribution of particle charges is then made smooth with the charge refinement algorithm.

After initialization at time t_0 the known variables are the particle positions $x(t_0)$, $x(t_0+a_t)$ and charges $Q(t_0)$, the currents $j_{x,i}(t_0+\frac{a_t}{2})$, the electric fields $E_{x,i}(t_0)$ and the gauge links $U_{x,i}(t_0+\frac{a_t}{2})$. The variables are then updated as follows:

(1) Compute the new electric field $E_{x,i}(t_0+a_t)$ via Eq. (2.10) using $j_{x,i}(t_0+\frac{a_t}{2})$ and $U_{x,i}(t_0+\frac{a_t}{2})$.
(2) Update $U_{x,i}(t_0+\frac{3a_t}{2})$ via Eq. (2.9) using $E_{x,i}(t_0+a_t)$.
(3) Update longitudinal particle positions via Eq. (2.13).
(4) Update particle charges $Q(t_0+a_t)$ according to either Eq. (2.17) or Eq. (2.19) (depending on sign of the particle velocity v) if a particle crosses a nearest-grid-point boundary.
(5) Interpolate charge density $\rho_x(t_0+a_t)$ using the NGP scheme and Eq. (2.15).
(6) Interpolate currents $j_{x,i}(t_0+\frac{3a_t}{2})$ using either Eq. (2.16) or Eq. (2.18) depending on sign of the particle velocity v.
(7) Compute various observables such as field energy, pressure components, etc.

This completes a simulation step.

III. NUMERICAL RESULTS

For all of our simulations [48] we use a model similar to the one proposed by McLerran and Venugopalan [4,5]. As discussed in Sec. II C, we consider charge distributions, which are random in the transversal direction, but correlated in the longitudinal direction. The randomly chosen color charge densities $\hat{\rho}^a_{1,2}(x_T)$ in the transversal plane are taken to be Gaussian with the correlation function

$$\langle \hat{\rho}^a_{1,2}(x_T)\hat{\rho}^b_{1,2}(y_T)\rangle = g^2\mu^2_{1,2}\delta^{(2)}(x_T-y_T)\delta^{ab}, \tag{3.1}$$

where the parameters $\mu_{1,2}$ control the variance of the fluctuating charges. McLerran and Venugopalan give an estimate of

$$\mu^2 = 1.1A^{1/3}\ \text{fm}^{-2}, \tag{3.2}$$

where A is the mass number of the colliding nuclei and the gauge group is SU(3). For $A=197$ (Au) we get

$$\mu \approx 0.505\ \text{GeV}. \tag{3.3}$$

We choose $g=2$ as common in CGC literature [10,13,47,49]. This leads to a realistic value for the saturation momentum Q_s,

$$Q_s \sim g^2\mu \sim 2\ \text{GeV}. \tag{3.4}$$

Even though our simulation is currently restricted to SU(2) for performance reasons, we still use this value to test our methods in semirealistic scenarios.

In all simulations we use Au-Au collisions as the standard case study, therefore μ is fixed. However, we vary other parameters such as the simulation volume, the nucleus width σ and IR and UV regulators. For example, using $N_T=128$ cells in the transversal directions and a lattice spacing of $a=0.028$ fm, the transversal area roughly covers 12.5% of the area of a single Au nucleus. In the longitudinal direction we could use $N_L=256$ cells, which covers a length of 5.2 fm. These are the parameters used in Sec. III A. For other parts of this paper we chose different parameter sets, which are specified in the corresponding sections.

We also have to choose the longitudinal thickness l of the nuclei, which is controlled by the longitudinal Gaussian width σ. In Sec. III A we show that $\sigma=4a_s$ is a good lower limit to avoid lattice artifacts. We approximate the thickness of the Gaussian profile by

$$l \approx 4\sigma. \tag{3.5}$$

Comparing the thickness l to the longitudinal extent of the Lorentz-contracted nucleus $\frac{2R_A}{\gamma}$, we obtain an estimate for the gamma factor γ:

$$\gamma = \frac{2R_A}{4\sigma} = \frac{R_A}{8a_s}, \tag{3.6}$$

where $R_A \approx 1.25A^{1/3}$ fm is the radius of a nucleus. With the values from above we get

$$\gamma \approx 45. \tag{3.7}$$

This value for γ corresponds to a center-of-mass energy of $\sqrt{s_{NN}} \approx 90$ GeV, however in the course of our paper we will demonstrate results obtained for $\gamma = 11$–455, corresponding to an energy range of $\sqrt{s_{NN}} = 20$–850 GeV. This energy range contains in particular parts of the parameter space explored by the low-energy Au + Au collisions at RHIC in the beam energy scan program with center-of-mass energies between $\sqrt{s_{NN}} = 7.7$–62.4 GeV [1].

For the solution of the Poisson equation in the transversal plane we employ IR and UV regularization as in Eq. (2.32). Infrared regularization leads to average color neutrality and suppresses long-range forces (e.g. monopoles and dipoles) on length scales m^{-1}. This is used to include effects of confinement in the classical simulation. The confinement

radius is roughly 1 fm, therefore one possibility is to set

$$m \approx (1\ \text{fm})^{-1} \approx 200\ \text{MeV} \approx \Lambda_{\text{QCD}}. \tag{3.8}$$

However we also work with values of up to 2 GeV to study the dependence of observables on the IR regulation. The UV cutoff Λ is introduced to eliminate high-momentum modes in the transversal plane whose dispersion relation on the lattice differs from the analytic case. Unless otherwise noted we use $\Lambda = 10$ GeV.

A. Comparison with boost-invariant initial conditions

It is important to check if the results produced by our $3+1$ dimensional simulations are similar to $2+1$ dimensional boost-invariant simulations, at least in the limit of thin nuclei. In the boost-invariant formulation it is natural to work with proper time $\tau = \sqrt{t^2 - z^2}$ and rapidity $\eta = \frac{1}{2}\ln\frac{t+z}{t-z}$ as coordinates for the forward light cone, where the collision event at $t = z = 0$ is used as the origin of the coordinate system. Note however that in collisions of nuclei with finite thickness, there is some ambiguity involved in choosing the space-time coordinates (t_c, z_c) of the collision. As a definition we set (t_c, z_c) to the space-time point of the maximum overlap of the Gaussian longitudinal profiles. The main advantage of this definition is that these coordinates are independent of the thickness parameter σ. To verify the agreement with the boost-invariant case, we compare the longitudinal chromoelectric fields created in our simulations to the fields, which are used as initial conditions for boost-invariant simulations. The boost-invariant initial conditions for the electric field at $\tau = 0^+$ created by the collision of charge densities of two nuclei $\hat{\rho}_1(x_T)$ and $\hat{\rho}_2(x_T)$ are given by [9]

$$E_L(x_T)|_{\tau=0^+} = -ig\sum_{i=1,2}[\alpha_1^i(x_T), \alpha_2^i(x_T)], \tag{3.9}$$

where $\alpha_{1,2}^i(x_T)$ is determined from the relations

$$e^{iga_s\alpha_{1,2}^i(x_T)} = e^{ig\hat{\varphi}_{1,2}^a(x_T)t^a}e^{-ig\hat{\varphi}_{1,2}^a(x_T+i)t^a}, \tag{3.10}$$

$$\Delta_T\hat{\varphi}_{1,2}^a(x_T) = -\hat{\rho}_{1,2}^a(x_T), \tag{3.11}$$

which are similar to our initial conditions in the laboratory frame: The first equation corresponds to Eq. (2.36), and the second one to the Poisson equation (2.25). This result is obtained in the Fock-Schwinger gauge $\tau A^\tau = 0$.

In our case the simulations start before the collision, where the nuclei are well separated in the longitudinal direction such that the gauge field in the center between them vanishes to numerical accuracy. The longitudinal chromoelectric fields which we want to compare to Eq. (3.9) are produced by numerically evolving the fields of the nuclei. We test our simulation as follows: We generate two initial charge densities $\hat{\rho}_{(1,2)}(x_T)$ and compute $\text{tr}E_L^2(x_T)|_{\tau=0^+}$, which is a gauge-invariant expression. Then we use the same charge densities to run a $3+1$ dimensional simulation with some finite nuclear thickness controlled by the Gaussian width σ. We record the energy density contribution of the longitudinal electric field $\text{tr}E_L^2(x_T)$ as a function of the transversal coordinate x_T during the collision in the central region $\eta = 0$. We then compute the correlation coefficient c between the numerical (simulation) result $\text{tr}E_L^2(x_T)_{\text{num}}$ and the analytic (boost-invariant) expression $\text{tr}E_L^2(x_T)_{\text{ana}}$ via

$$c(\text{tr}(E_L^2)_{\text{num}}, \text{tr}(E_L^2)_{\text{ana}}) \equiv \frac{\text{cov}(\text{tr}(E_L^2)_{\text{num}}, \text{tr}(E_L^2)_{\text{ana}})}{\sigma_{\text{num}}\sigma_{\text{ana}}}, \tag{3.12}$$

where the covariance across the transversal plane is defined by

$$\text{cov}(\text{tr}(E_L^2)_{\text{num}}, \text{tr}(E_L^2)_{\text{ana}}) = \sum_{x_T}(\text{tr}E_L^2(x_T)_{\text{num}} - \overline{\text{tr}(E_L^2)_{\text{num}}}) \times (\text{tr}E_L^2(x_T)_{\text{ana}} - \overline{\text{tr}(E_L^2)_{\text{ana}}}), \tag{3.13}$$

with the mean values $\overline{\text{tr}(E_L^2)}_{(\text{num,ana})}$ and the standard deviations $\sigma_{(\text{num,ana})}$ associated with $\text{tr}E_L^2(x_T)_{\text{num}}$ and $\text{tr}E_L^2(x_T)_{\text{ana}}$ respectively. The mean and standard deviation are understood to be computed across the transversal plane. A plot of the energy densities $\text{tr}E_L^2(x_T)$ for different widths is shown in Fig. 4.

The correlation between the numerical and analytical results is recorded as a function of time, the nuclear thickness σ and the UV cutoff Λ. The results for a single event as a function of σ are shown in Fig. 5 (left panel): The blue (lower) curve corresponds to the fixed time t_c where the two nuclei overlap completely. We see that the correlation increases for thinner widths σ, but at a certain point around $\sigma \approx 3a_s$ the correlation is reduced due to discretization errors. Very thin longitudinal profiles tend to disperse, produce unphysical longitudinal fields even before the collision and eventually become unstable. This is because thin widths cannot be properly resolved on the lattice below a certain threshold. To ensure numerical stability we deduce a minimum width of $\sigma_{\text{min}} = 4a_s$ for the nuclear thickness in our simulations. We remark that very fine lattices with small (in physical units) lattice spacings are required to accurately simulate thin nuclei on the lattice.

The red (upper) curve in Fig. 5 on the left is the maximum value of the correlation during the collision. We see that thicker nuclei also produce fields which are similar to the boost-invariant case (thus leading to higher correlations), but at earlier times than t_c. This happens because they start to overlap much earlier, producing the characteristic longitudinal electric fields. The time

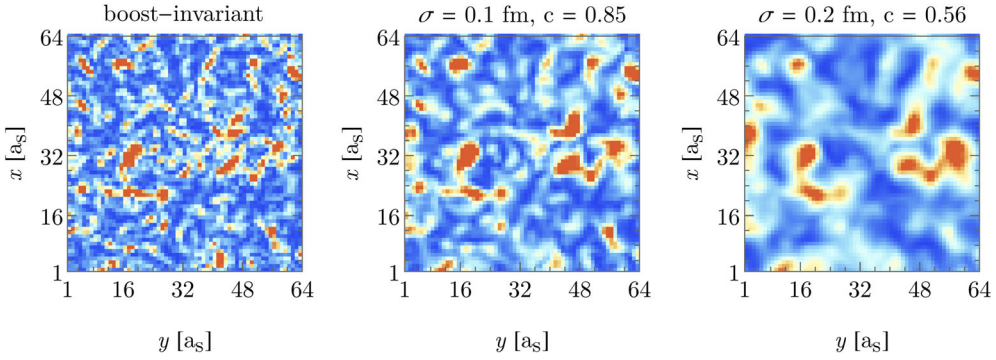

FIG. 4. Density plot of the energy density component $\mathrm{tr}E_L^2(x_T)$ as a function of the transverse coordinate $x_T = (x, y)$ in the center region of the collision for a single event. The left panel shows the boost-invariant ("analytic") result for $\tau = 0^+$. The middle and right panels show the simulation results for two different values of the thickness parameter σ. The correlation coefficient c quantifies how similar the energy density distributions are to the boost-invariant case. Thinner nuclei (middle) lead to a correlation coefficient of $c = 0.85$, whereas the energy density distributions of thicker nuclei (right) are more washed out with lower values of $c = 0.56$. The grid size $N_L \cdot N_T^2$ of the simulation is set to $256 \cdot 128^2$ with a lattice spacing of $a_s = 0.028$ fm and a time step of $a_t = a_s/2$. The IR regulator is set to $m = 2$ GeV and the UV cutoff is $\Lambda = 10$ GeV. The transversal area covers 12.5% of the full area of a single Au nucleus, but we only show a quarter of the area to make the similarities visually more obvious.

evolution from the onset of the overlap to the full overlap at t_c changes the fields, resulting in low values of the correlations at t_c.

In Fig. 5 (right panel) we study the effects of the IR regulator m and the UV cutoff Λ on our results by fixing the width σ and varying the values of m and Λ. We see that cutting off high momentum modes whose dispersion relation differs from the continuum case increases the correlation with the analytic result. Regulating the UV modes becomes necessary because in the MV model all available modes in momentum space are populated up to the lattice cutoff scale Λ_{latt}. Increasing the resolution of the simulation box without regulating the UV modes does not lead to any improvement.

We also observe that the correlation coefficient is largely independent of the IR regulator m. However, lower values of m decrease the correlation significantly in the same manner as small values of σ do. Small m boosts the amplitudes of the low momentum modes of $\hat{\varphi}^a(x_T)$ [as is apparent from Eq. (2.32)], which drives the same

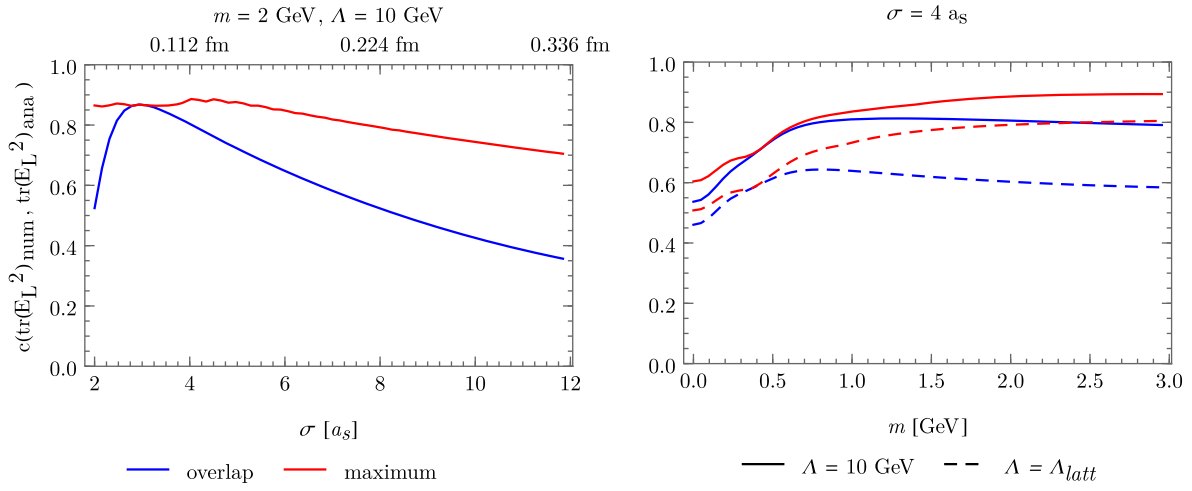

FIG. 5. Comparison of simulations to boost-invariant initial conditions. This plot shows the correlation coefficient of $\mathrm{tr}E_L^2(x_T)_{\mathrm{num}}$ in the central region with the boost-invariant result for $\mathrm{tr}E_L^2(x_T)_{\mathrm{ana}}$ at $\tau = 0^+$ as a function of σ and m. A correlation coefficient of 1 implies perfect agreement between the numerical and the analytical result. The blue solid line shows the correlation when the nuclei completely overlap and the red line is the maximum correlation achieved during the evolution. The correlation increases for thinner nuclei. Small values of m and σ lead to decreased correlations due to numerical instabilities, which appear at high field amplitudes. The simulation parameters are the same as in Fig. 4 except that we vary the thickness parameter σ and IR regulator m. Left panel: Correlations as a function of the thickness parameter σ. Right panel: Correlations as a function of the IR regulator m. For the thick curves we used $\Lambda = 10$ GeV as a UV cutoff. Dashed lines use the UV cutoff Λ_{latt} given by the lattice.

numerical instability we see when using very small values of σ. This instability can be cured by using finer grids (i.e. smaller lattice spacings a_s) while keeping the volume of the simulation box and all other physical parameters fixed. A smaller lattice spacing a_s for the same physical volume of the box brings the gauge links $U_{x,i}$ closer to the group identity element **1** and consequently the lattice approximations of the fields become more accurate. We note that this instability is of numerical nature only and also appears in the evolution of a single nucleus without any collision.

Studying the correlation between our numerical results and the analytic expressions for the boost-invariant initial conditions shows that we are able to correctly describe boost-invariant collisions in the limit of thin nuclei. However it also reveals that one has to be careful in choosing simulation parameters, in particular $\sigma \gtrsim 4a_s$. To describe Au-Au collisions in our simulation framework we work with an IR regulator of $m = 2$ GeV (which is of the order of the saturation momentum) and a UV cutoff $\Lambda = 10$ GeV (which is used to cut off high momentum modes not satisfactorily described on the lattice). These parameters are used in the following sections unless otherwise noted.

B. Pressure anisotropy

A prominent phenomenon in the early stages of heavy-ion collisions is the pressure anisotropy of the glasma fields and the subsequent isotropization of the system. The main observables in this context are the transversal and longitudinal pressure components $p_T = \varepsilon_L$ and $p_L = \varepsilon_T - \varepsilon_L$ with the longitudinal and transversal energy density components given by

$$\varepsilon_L = \frac{1}{2}(E_z^a E_z^a + B_z^a B_z^a), \tag{3.14}$$

$$\varepsilon_T = \frac{1}{2}\sum_{i=x,y}(E_i^a E_i^a + B_i^a B_i^a). \tag{3.15}$$

Our simulation framework enables us to compute the pressure components as functions of time t and the longitudinal and transverse coordinates z and x_T. To simplify we average over x_T, which is natural within the MV model. A plot of the pressure components in the laboratory frame at different times is shown in Fig. 6. The initially purely transverse fields of the incoming nuclei manifest themselves as large Gaussian bumps in the longitudinal pressure component. During the collision the transverse pressure component builds up and remains largely flat afterwards. The longitudinal pressure in the laboratory frame falls off exponentially towards the center of the collision. In order to better compare our results to the boost-invariant case it is sensible to switch to the comoving frame described by proper time $\tau = \sqrt{t^2 - z^2}$ and rapidity $\eta = \frac{1}{2}\ln\frac{t+z}{t-z}$. We choose the space-time coordinates (t_c, z_c) of the collision as in Sec. III A.

By introducing the longitudinal component of the Poynting vector

$$S_L \equiv 2\mathrm{tr}(\vec{E} \times \vec{B})_z, \tag{3.16}$$

we can compute the transformed longitudinal pressure

$$\bar{p}_L(\tau,\eta) = p_L(\tau,\eta)\cosh^2\eta + \varepsilon(\tau,\eta)\sinh^2\eta - 2S_L(\tau,\eta)\cosh\eta\sinh\eta. \tag{3.17}$$

The transverse pressure component is unaltered by the coordinate transformation. A plot of the longitudinal pressure $\bar{p}_L(\tau,\eta)$ in the comoving frame is shown in Fig. 7. It reveals that at early times $\bar{p}_L$ is still largely influenced by the tails of the colliding nuclei. At later times $\bar{p}_L$ becomes flat in the midrapidity region, which is consistent with approximate boost invariance. We have to keep in mind that within our simulations the observables we compute are always slightly influenced by the initial fields of the nuclei, especially at early proper times.

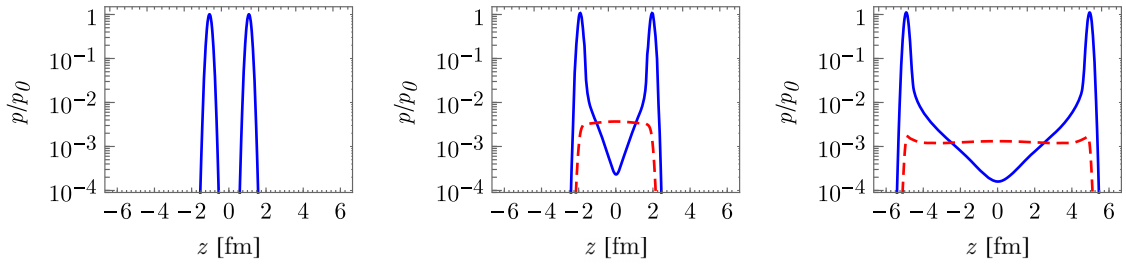

FIG. 6. Longitudinal and transverse pressure components as functions of the longitudinal coordinate z in the laboratory frame at different times t before and after the collision. The coordinate origin is centered around the collision event at $t = 0$ and $z = 0$. The blue curve describes the longitudinal pressure $p_L(z)$ and the red dashed curve is the transverse pressure component $p_T(z)$. The longitudinal chromoelectric and chromomagnetic fields characteristic for the glasma contribute to the transverse pressure p_T. The pressure components are normalized to the maximum longitudinal pressure p_0 of the initial nuclei. For these plots we use a grid size of 320×256^2 with a lattice spacing of $a_s = 0.04$ fm and a time step of $a_t = \frac{a_s}{2}$. The thickness parameter is set to $\sigma = 4a_s$ (which corresponds to a gamma factor of $\gamma \approx 23$), the IR regulator is set to $m = 2$ GeV and the UV cutoff is set to $\Lambda = 10$ GeV. Left panel: Before the collision: $t = -1$ fm/c. Middle panel: After the collision: $t = 2$ fm/c. Right panel: $t = 5$ fm/c.

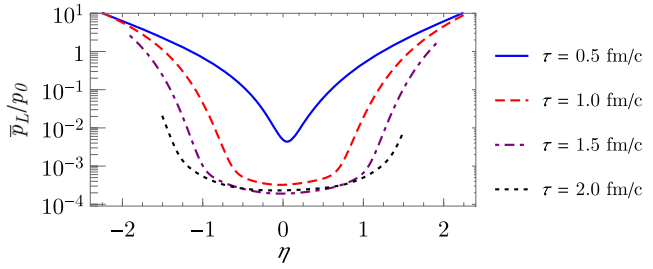

FIG. 7. Longitudinal pressure component $\bar{p}_L(\eta)$ in the comoving frame as a function of rapidity η for different proper times τ. At later times the longitudinal pressure becomes flat within the rapidity interval $(-1, 1)$. Even though the nuclei in this simulation are relatively thick ($\gamma \approx 23$) we still recover approximate boost invariance. For these plots we use the same simulation parameters as in Fig. 6.

We now turn towards studying the pressure anisotropy. For the further analysis it will be sufficient to stay in the central region $\eta = 0$. In the boost-invariant case the initial glasma fields at $\tau = 0^+$ are made of purely longitudinal color flux tubes, which leads to highly anisotropic initial pressures $p_T|_{\tau=0^+} = \varepsilon_L|_{\tau=0^+}$ and $p_L|_{\tau=0^+} = -\varepsilon_L|_{\tau=0^+}$. As the flux tubes expand, they generate transversal electric and magnetic fields until $\varepsilon_L \simeq \varepsilon_T$ and $p_L \simeq 0$ [50]. This is the free-streaming limit observed in boost-invariant CGC simulations and stands in contrast to the observation of an isotropized quark-gluon plasma where $p_T \simeq p_L$ after a few fm/c [51,52]. It has been shown that boost-invariance breaking fluctuations drive instabilities in the glasma, which can move the system towards isotropization [12–14]. In our simulations we explicitly violate boost invariance by introducing a finite nucleus thickness. It is therefore interesting to investigate the effects of the thickness parameter σ on the pressure anisotropy of the glasma.

For our numerical studies it is convenient to introduce the pressure to energy density ratios $\frac{p_T}{\varepsilon}$ and $\frac{p_L}{\varepsilon}$ with $\varepsilon = \varepsilon_L + \varepsilon_T$. The free-streaming limit then corresponds to $\frac{p_T}{\varepsilon} \simeq \frac{1}{2}$ and $\frac{p_L}{\varepsilon} \simeq 0$. Isotropization would be signaled by $\frac{p_T}{\varepsilon} \simeq \frac{p_L}{\varepsilon} \simeq \frac{1}{3}$. Both the pressure and energy density components are averaged over the transverse plane and 32 events are used for the statistical sampling. We choose a grid size of 320 cells in the longitudinal direction and 256^2 cells to resolve the transversal area. For collisions of thick nuclei in Fig. 8 (left panel) we choose a lattice spacing of $a_s = 0.04$ fm. The transversal grid then covers the full area πR_A^2 of a gold nucleus.

For simulations of thin nuclei in Fig. 8 (right panel) we are forced to use smaller lattice spacings of $a_s = 0.008$ fm (for $\sigma = 0.032$ fm), $a_s = 0.004$ fm (for $\sigma = 0.016$ fm) and $a_s = 0.002$ fm (for $\sigma = 0.008$ fm), because grids much larger than 320×256^2 as used here currently exceed our available computational resources. The transversal area then only covers 4%, 1% and 0.25% of the full area respectively. The temporal spacing is set to $a_t = \frac{a_s}{2}$.

The results are shown in Fig. 8 and there are several observations we make:

(1) From Fig. 8 (left panel) we see that we recover the free-streaming limit of the boost-invariant case. Isotropization is not reached within possible simulation times due to limitations from both the longitudinal and transversal simulation box size. We can observe slight movement of both pressure components towards the desired value of $\frac{1}{3}$, but not within any realistic time scales.

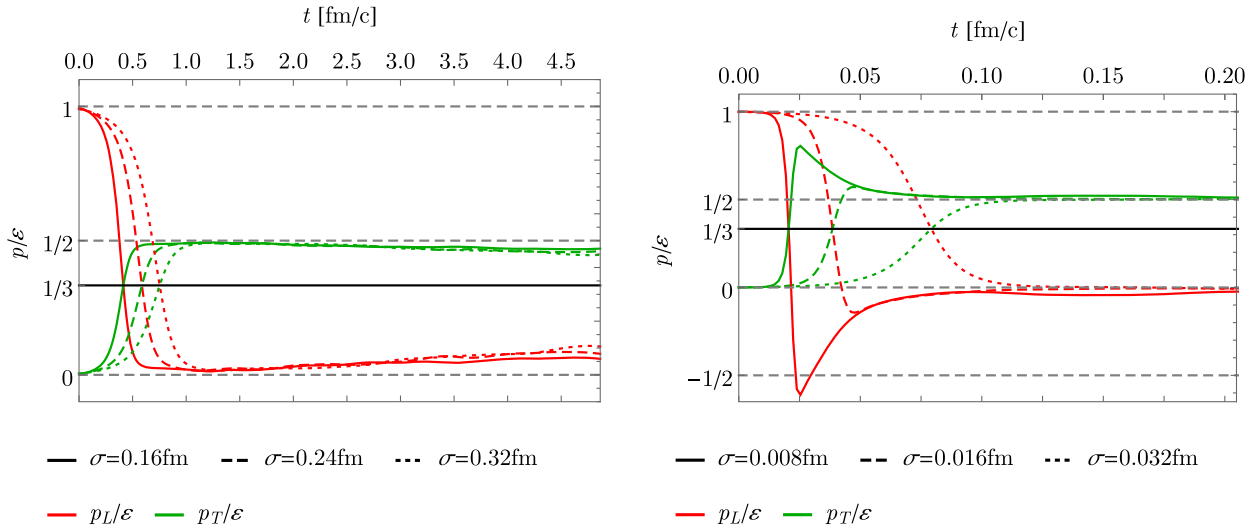

FIG. 8. Longitudinal and transversal pressure components in the central region $\eta = 0$ as a function of time for various nuclear thicknesses σ. An IR regulator of $m = 2$ GeV and a UV cutoff of $\Lambda = 10$ GeV has been used. The detailed simulation parameters are explained in the Sec. III B. Left panel: Pressure components for thick nuclei. Right panel: Pressure components for thin nuclei.

(2) The initial pressures directly after the collision behave differently compared to the boost-invariant case. In our simulations of thick nuclei in Fig. 8 (left panel) we see that in the beginning p_L dominates p_T due to the presence of the transverse fields of the colliding nuclei. As the nuclei recede from the collision volume the created glasma fields have already reached the free-streaming limit and therefore no negative longitudinal pressures are observed.

(3) In the results for thin nuclei in Fig. 8 (right panel) we can recover negative longitudinal pressure. The colliding nuclei move away from the collision center fast enough, leaving behind longitudinal color flux tubes, which have not decayed yet. The still largely longitudinal fields generate negative pressure, which is characteristic for the early glasma phase.

We remark here that our ansatz for the initial conditions relies on an assumption about the longitudinal structure of the nuclei. The initial conditions described in Sec. II C imply correlation of the charge density in the longitudinal direction of order σ and correlation in the transversal direction of order m^{-1}. The charge distribution is random in the transversal direction, but there is no random longitudinal structure. As a consequence we were able to drop the time ordering in Eq. (2.30). However, it has been shown that random longitudinal structure (which demands proper path/time ordering) in the initial nucleus fields—among other effects—leads to higher initial energy densities in the glasma [47]. Additional longitudinal randomness might also give rise to larger deviations from the boost-invariant case after the collision. This could be similar to boost-invariance breaking perturbations of the glasma, which cause plasma instabilities that have been found to accelerate isotropization [12–14]. It is therefore conceivable to expect that implementing this random longitudinal structure in our initial conditions will change the results and could lead to faster isotropization times. Detailed understanding of these issues requires an analysis of gluon occupation numbers in momentum space and their temporal behavior. We plan to investigate this in a future publication.

C. Energy production

One of the fundamental assumptions made in the CGC framework is the separation of hard and soft degrees of freedom, which are modeled as external color charges and classical gauge fields respectively. As a result of the collision there is an energy exchange between the charges and the fields. However, since the nuclei are assumed to be recoilless, the hard sector acts as an inexhaustible energy reservoir for the gauge fields. The resulting field energy increase can be interpreted as the work done by the charges against the field. In the boost-invariant case this effect is implicitly included in the initial conditions for the fields at $\tau = 0^+$. In our approach we are able to explicitly compute the energy increase during and after the collision. The change of the total field energy density ε as a function of time can be formulated in terms of an energy continuity equation,

$$\frac{d\varepsilon}{dt} + \frac{1}{V}\int \partial_i S_i d^3x + \frac{1}{V}\int E_i^a J_i^a d^3x = 0, \tag{3.18}$$

which is the non-Abelian version of the Poynting theorem. The time dependence of ε is governed by two terms: the components S_i of the Poynting vector $S_j \equiv 2\mathrm{tr}(\vec{E}\times\vec{B})_j$ and $E_i^a J_i^a$. The integral over the total derivative of the Poynting vector can be omitted in the continuum. On the lattice this term only gives a negligible contribution due to discretization errors. In the scalar product $E_i^a J_i^a$ the only nonvanishing part of the current J_i^a is the longitudinal component J_z^a and therefore the expression reduces to $E_z^a J_z^a$. Consequently, the energy production is caused by longitudinal chromoelectric fields in the glasma and must be centered around the collision event and the boundary of the forward light cone where the color currents are nonzero.

The energy increase as a function of time is shown in Fig. 9. We observe that the total energy density is conserved before the onset of the collision when the external charges and the classical fields describing both nuclei are propagating through vacuum. Afterwards there is a strong energy increase during as well as after the collision. At later times there is an ongoing, but slowly decreasing energy production, which finally becomes almost constant. To check the stability of our results with respect to a change in the spatial and temporal resolution of the grid we vary the spatial lattice spacing a_s and the time step a_t. Overall there is a good agreement between results at different discretizations. The violation of Eq. (3.18) is small and can be further reduced using smaller time steps as seen in the lower plot of Fig. 9.

D. Suppression of longitudinal chromomagnetic fields

In the following we investigate the production of longitudinal chromomagnetic fields B_L^a and chromoelectric fields E_L^a characteristic for the glasma at early times. In the boost-invariant case the contributions to the energy density from magnetic and electric color flux tubes ($\mathrm{tr}B_L^2$ and $\mathrm{tr}E_L^2$ respectively) should be equal after averaging over initial conditions. In our simulations with finite σ we observe that this is not the case and there is a dependency on the thickness parameter σ as well as the IR regulator m. The results are presented in Figs. 10 and 11.

Figure 10 shows the ratio of magnetic and electric longitudinal fields $\langle \mathrm{tr}B_L^2\rangle / \langle \mathrm{tr}E_L^2\rangle$ in the central region ($\eta = 0$) for a range of values of the nucleus thickness σ and an IR regulator $m = 2$ GeV. Collisions of thick nuclei show a very small ratio of about 0.1–0.2 after the collision. In the case of thin nuclei in Fig. 10 (right panel) the ratio

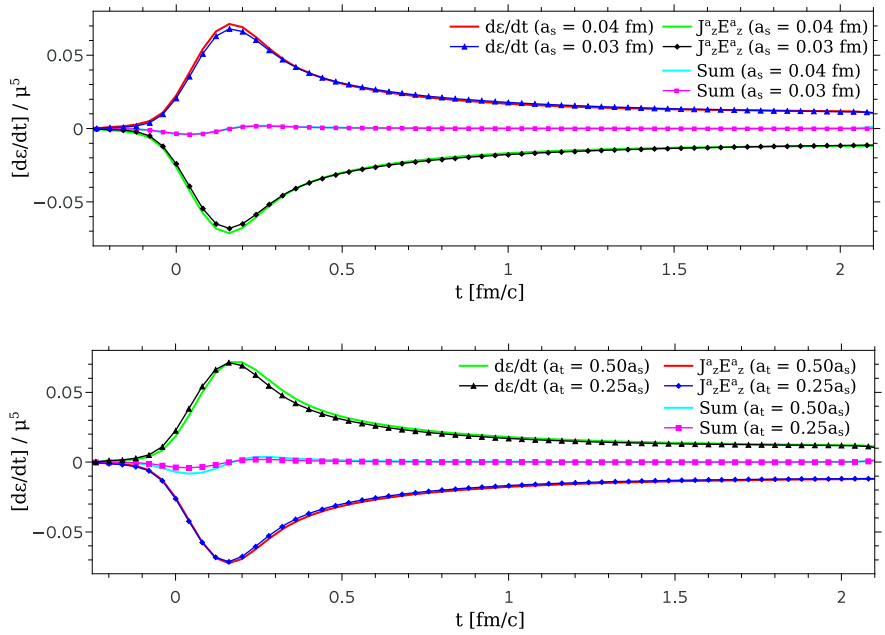

FIG. 9. Energy production as a function of time with different spatial and temporal discretizations. The "Sum" curves correspond to the left-hand side of Eq. (3.18). Their deviation from zero is a consequence of lattice artifacts and can be reduced by using finer time discretizations. The results have been obtained on a cubic lattice with a fixed volume of $(5.12\ \mathrm{fm})^3$ with the IR regulator set to $m = 1$ GeV and an UV cutoff $\Lambda = 10$ GeV. The nuclear thickness σ was set to 0.16 fm. We averaged over ten configurations in order to have a sufficient statistical sample. Upper panel: Varying spatial discretization by keeping $a_t = 0.01\ \mathrm{fm}/c$ fixed. Lower panel: Varying temporal discretization by keeping $a_s = 0.04$ fm fixed.

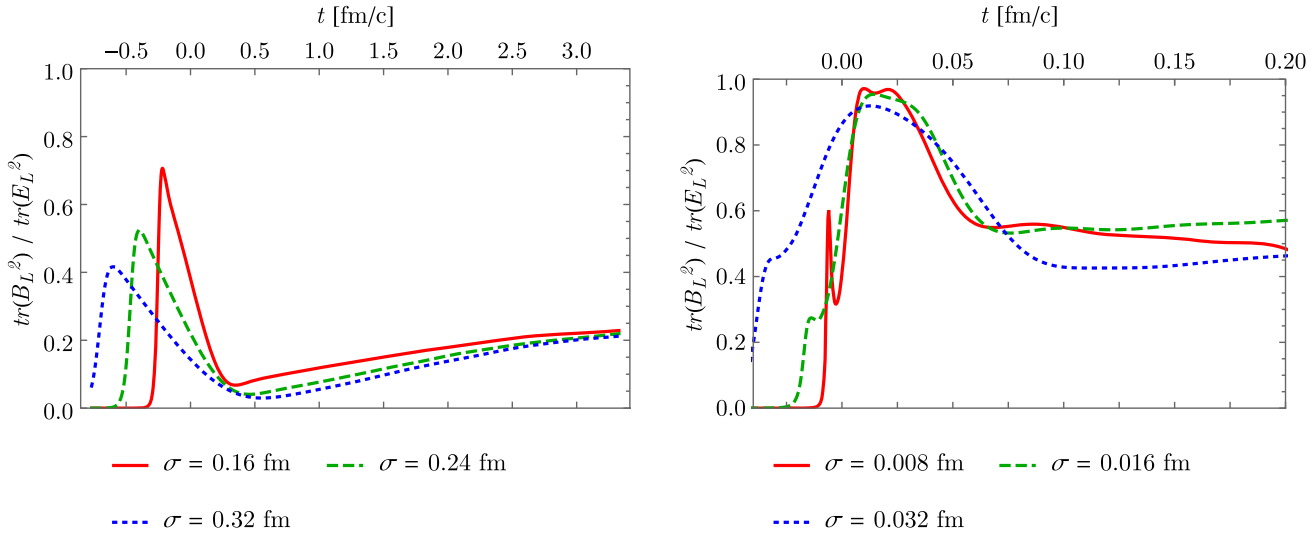

FIG. 10. Ratio of magnetic to electric longitudinal energy density contributions as a function of time for various nuclear thicknesses σ. The ratio increases for thin nuclei, but magnetic flux tubes are still heavily suppressed compared to the boost-invariant scenario. The simulation parameters are the same as in Sec. III B. Left panel: Ratio of longitudinal energy density components for thick nuclei. Right panel: Ratio of longitudinal energy density components for thin nuclei.

increases to roughly ~0.5, which is still far away from the "canonical" value of 1 in the boost-invariant scenario. Note that due to the small physical volumes used in the simulations of thin nuclei it is harder to achieve adequate statistics. As a result, the curves in Fig. 10 in the right panel are not as smooth as in the left panel.

The results do not only depend on the thickness σ. In Fig. 11 the results are shown for a fixed nuclear thickness $\sigma = 0.08$ fm ($\gamma \approx 45$) and a varying IR regulator.[3] We

[3]We remark that varying the IR regulator m has only a weak influence on the pressure anisotropy.

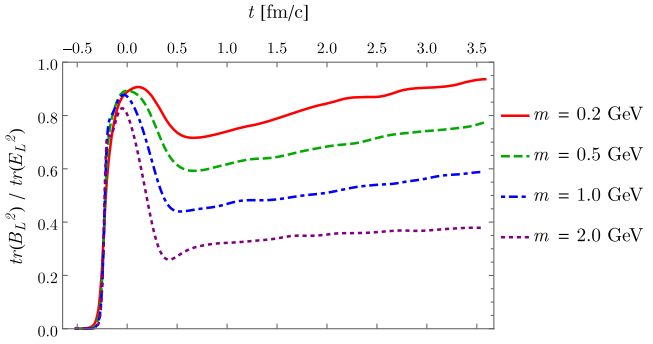

FIG. 11. Ratio of magnetic to electric longitudinal energy density contributions as a function of time for various values of the IR regulator m. For this plot we used a grid size of 256^3 cells with a lattice spacing $a_s = 0.02$ fm and averaged over 32 events. The transversal area covers 25% of the full area of a gold nucleus. The thickness parameter is set to $\sigma = 0.08$ fm, which corresponds to $\gamma \approx 45$. We approach the boost-invariant limit for small m.

observe that reducing m to 200 MeV (which roughly corresponds to a correlation length of the color fields of the order of the confinement radius 1 fm) leads to better agreement with the boost-invariant case with a ratio of ∼0.8. Note that this dependency of the ratio of magnetic and electric longitudinal fields on the IR regulator m is not present in the boost-invariant initial conditions [9].

The presented results seemingly suggest a suppression of chromomagnetic flux tubes (or an overproduction of chromoelectric flux tubes) in the glasma phase when introducing a finite nucleus thickness. However, the strong dependency of the magnetic to electric longitudinal field ratio on the IR regulator m leads us to suspect that this discrepancy between our simulations and the boost-invariant case is an artifact, which can be attributed to the initial conditions introduced in Sec. II C. As already mentioned there and in Sec. III B the longitudinal structure of our nuclei does not include "longitudinal randomness." Consequently, the typical color structures in our initial conditions have a thickness proportional to σ and a transversal width of the order of m^{-1}. To be consistent with the picture of a highly Lorentz-contracted nucleus modeled by classical Yang-Mills fields one would demand that $\sigma m \ll 1$, such that nucleons within the nucleus are also contracted to flat "pancakes." Therefore, if we move away from the limit $\sigma m \ll 1$, we can expect to see deviations from the boost-invariant case, but these deviations may very well solely be due to the longitudinal coherence. This reasoning is consistent with our simulation results: In the case of a thickness of $\sigma = 0.16$ fm with an IR regulator of $m = 2$ GeV the longitudinal magnetic fields are weakened as seen in Fig. 10. Here we have a value of $\sigma m = 1.6$, which corresponds to color structures which are prolonged in the longitudinal direction. We can compare this to the case of $\sigma = 0.08$ fm and $m = 200$ MeV as presented in Fig. 11. The ratio of magnetic to electric fields is closer to 1 and at the same time we have $\sigma m = 0.08$, which can be considered small.

Including random longitudinal structure in the nuclei as suggested in [47] will help to clarify, if suppressed longitudinal magnetic fields are a physical consequence of a finite thickness or if the suppression is just an artifact of our ansatz. However with the reasoning presented above we suspect that this effect will disappear for more realistic initial conditions.

IV. CONCLUSION

In this work we have simulated heavy-ion collisions in the laboratory frame with thick nuclei in the McLerran-Venugopalan model. Finite thickness in the longitudinal direction allows the simulation of collisions at lower energies, but requires abandoning boost invariance in the calculation as well as including nontrivial color source evolution in the simulation. Both can be readily implemented using CPIC in the laboratory frame. With our framework we are able to access a range of nuclear thicknesses down to those corresponding to center-of-mass energies as used in the low-energy beam energy scan program of RHIC and up to LHC energies.

We started from an analytic solution of a non-Abelian random color current sheet of finite extent in the longitudinal direction and the corresponding field configuration that propagate at the speed of light. The discretization of this solution on a grid requires refining the charge distribution on sublattice resolution. For the interpolation between particles and fields, we utilized the nearest-grid-point method as a charge conserving interpolation scheme. A distinct feature of our approach is the possibility to explicitly compute the energy, which is pumped into the Yang-Mills fields by the propagating color charges. We verified that the energy increase correctly satisfies the Poynting theorem for non-Abelian fields.

We compared calculations in the laboratory frame with results from boost-invariant approaches. Concentrating on gauge-invariant observables, we see that the correlation of initial conditions right after the collision increases for thinner nuclei, which means that boost invariance is restored in this limit. We computed the components of the energy-momentum tensor, especially focusing on the pressure parallel and perpendicular to the propagation direction. We show that our pressure distributions in laboratory frame coordinate space correspond to largely rapidity-independent pressure distributions in Bjorken coordinates for the midrapidity region. Our results confirm the previous findings, which established the picture of strongly pronounced pressure anisotropy during the very early phase of the fireball evolution.

For thicker nuclei we find the following deviations: There is a suppression of the chromomagnetic longitudinal components of the energy-momentum tensor with respect to their chromoelectric counterparts. We analyzed this

phenomenon and determined its dependence on the thickness parameter and the IR regulator. Regarding pressure components, we observe a slow tendency towards isotropization in our simulations. A more detailed future investigation including random longitudinal structure in our model could potentially further reduce isotropization times.

Other possible and planned improvements are the extraction of particle spectra in order to compare with experimentally measured multiplicities and also some rather technical aspects, like improved interpolation prescriptions, which could be beneficial to widen the scope of parameters accessible to our numerical approach. Another step towards a more realistic simulation of QCD processes in heavy-ion collisions at low collision energies would be the inclusion of backreaction of the classical gauge fields onto the color charges. In the future the CPIC framework could also allow us to take interactions and scatterings between the hard constituents of both nuclei into account. Such steps, however, would go beyond the usual assumptions of the CGC effective theory and may require an improved understanding of the internal nuclear structure.

ACKNOWLEDGMENTS

This work has been supported by the Austrian Science Fund FWF, Project No. P 26582-N27 and Doctoral program No. W1252-N27. The computational results presented have been achieved using the Vienna Scientific Cluster (VSC). We would like to thank Anton Rebhan, Sören Schlichting, Andreas Schmitt and Raju Venugopalan for useful discussions.

[1] L. Adamczyk *et al.* (STAR Collaboration), Elliptic flow of identified hadrons in Au + Au collisions at $\sqrt{s_{NN}} = 7.7$–62.4 GeV, Phys. Rev. C **88**, 014902 (2013).
[2] E. Iancu, A. Leonidov, and L. McLerran, The color glass condensate: An introduction, in QCD perspectives on hot and dense matter, *NATO Advanced Study Institutes, Summer School, Cargese, France, 2001* (Kluwer Academic, Dordrecht, 2002), pp. 73–145.
[3] E. Iancu, Gluon saturation at small x, in *Multiparticle dynamics, Proceedings of the 31st International Symposium, ISMD 2001, Datong, China, 2001* (World Scientific, River Edge, 2002), pp. 184–191.
[4] L. D. McLerran and R. Venugopalan, Gluon distribution functions for very large nuclei at small transverse momentum, Phys. Rev. D **49**, 3352 (1994).
[5] L. McLerran and R. Venugopalan, Computing quark and gluon distribution functions for very large nuclei, Phys. Rev. D **49**, 2233 (1994).
[6] B. Schenke, P. Tribedy, and R. Venugopalan, Event-by-event gluon multiplicity, energy density, and eccentricities in ultrarelativistic heavy-ion collisions, Phys. Rev. C **86**, 034908 (2012).
[7] B. Schenke, P. Tribedy, and R. Venugopalan, Fluctuating Glasma Initial Conditions and Flow in Heavy Ion Collisions, Phys. Rev. Lett. **108**, 252301 (2012).
[8] F. Gelis, Color glass condensate and glasma, Int. J. Mod. Phys. A **28**, 1330001 (2013).
[9] A. Krasnitz and R. Venugopalan, Nonperturbative computation of gluon minijet production in nuclear collisions at very high energies, Nucl. Phys. **B557**, 237 (1999).
[10] T. Lappi, Production of gluons in the classical field model for heavy ion collisions, Phys. Rev. C **67**, 054903 (2003).
[11] A. Kovner, L. D. McLerran, and H. Weigert, Gluon production from non-Abelian Weizsäcker-Williams fields in nucleus-nucleus collisions, Phys. Rev. D **52**, 6231 (1995).
[12] T. Epelbaum and F. Gelis, Pressure Isotropization in High Energy Heavy Ion Collisions, Phys. Rev. Lett. **111**, 232301 (2013).
[13] K. Fukushima and F. Gelis, The evolving glasma, Nucl. Phys. **A874**, 108 (2012).
[14] J. Berges and S. Schlichting, The nonlinear glasma, Phys. Rev. D **87**, 014026 (2013).
[15] B. Schenke, P. Tribedy, and R. Venugopalan, Multiplicity distributions in p + p, p + A and A + A collisions from Yang-Mills dynamics, Phys. Rev. C **89**, 024901 (2014).
[16] B. Schenke, S. Schlichting, and R. Venugopalan, Azimuthal anisotropies in p + Pb collisions from classical Yang-Mills dynamics, Phys. Lett. B **747**, 76 (2015).
[17] K. Dusling and R. Venugopalan, Azimuthal anisotropy from color glass condensates in proton-nucleus collisions, Nucl. Phys. **A931**, 283 (2014).
[18] D. Gelfand, F. Hebenstreit, and J. Berges, Early quark production and approach to chemical equilibrium, Phys. Rev. D **93**, 085001 (2016).
[19] J. Berges, D. Gelfand, S. Scheffler, and D. Sexty, Simulating plasma instabilities in SU(3) gauge theory, Phys. Lett. B **677**, 210 (2009).
[20] J. Berges, K. Boguslavski, S. Schlichting, and R. Venugopalan, Universal attractor in a highly occupied non-Abelian plasma, Phys. Rev. D **89**, 114007 (2014).
[21] P. Romatschke and R. Venugopalan, The unstable glasma, Phys. Rev. D **74**, 045011 (2006).
[22] J. Berges, B. Schenke, S. Schlichting, and R. Venugopalan, Turbulent thermalization process in high-energy heavy-ion collisions, Nucl. Phys. **A931**, 348 (2014).
[23] A. Ipp, A. Rebhan, and M. Strickland, Non-Abelian plasma instabilities: SU(3) vs SU(2), Phys. Rev. D **84**, 056003 (2011).
[24] P. Romatschke and A. Rebhan, Plasma Instabilities in an Anisotropically Expanding Geometry, Phys. Rev. Lett. **97**, 252301 (2006).

[25] A. Rebhan, M. Strickland, and M. Attems, Instabilities of an anisotropically expanding non-Abelian plasma: 1D + 3V discretized hard-loop simulations, Phys. Rev. D **78**, 045023 (2008).
[26] A. Rebhan and D. Steineder, Collective modes and instabilities in anisotropically expanding ultrarelativistic plasmas, Phys. Rev. D **81**, 085044 (2010).
[27] M. Attems, A. Rebhan, and M. Strickland, Instabilities of an anisotropically expanding non-Abelian plasma: 3D + 3V discretized hard-loop simulations, Phys. Rev. D **87**, 025010 (2013).
[28] J.-P. Blaizot, F. Gelis, J.-F. Liao, L. McLerran, and R. Venugopalan, Bose-Einstein condensation and thermalization of the quark gluon plasma, Nucl. Phys. **A873**, 68 (2012).
[29] M. C. Abraao York, A. Kurkela, E. Lu, and G. D. Moore, UV cascade in classical Yang-Mills theory via kinetic theory, Phys. Rev. D **89**, 074036 (2014).
[30] A. Kurkela and E. Lu, Approach to Equilibrium in Weakly Coupled Non-Abelian Plasmas, Phys. Rev. Lett. **113**, 182301 (2014).
[31] A. Kurkela and Y. Zhu, Isotropization and Hydrodynamization in Weakly Coupled Heavy-Ion Collisions, Phys. Rev. Lett. **115**, 182301 (2015).
[32] G. Chen, R. J. Fries, J. I. Kapusta, and Y. Li, Early time dynamics of gluon fields in high energy nuclear collisions, Phys. Rev. C **92**, 064912 (2015).
[33] M. Li and J. I. Kapusta, Pressure isotropization in heavy ion collisions from color glass condensate, arXiv:1602.09060.
[34] R. J. Fries, J. I. Kapusta, and Y. Li, Near-fields and initial energy density in the color glass condensate model, arXiv:nucl-th/0604054.
[35] J. Kogut and L. Susskind, Hamiltonian formulation of Wilson's lattice gauge theories, Phys. Rev. D **11**, 395 (1975).
[36] S. Wong, Field and particle equations for the classical Yang-Mills field and particles with isotopic spin, Nuovo Cimento A **65**, 689 (1970).
[37] J. P. Verboncoeur, Particle simulation of plasmas: Review and advances, Plasma Phys. Controlled Fusion **47**, A231 (2005).
[38] C. Hu and B. Müller, Classical lattice gauge field with hard thermal loops, Phys. Lett. B **409**, 377 (1997).
[39] G. D. Moore, C.-r. Hu, and B. Müller, Chern-Simons number diffusion with hard thermal loops, Phys. Rev. D **58**, 045001 (1998).
[40] A. Dumitru, Y. Nara, and M. Strickland, Ultraviolet avalanche in anisotropic non-Abelian plasmas, Phys. Rev. D **75**, 025016 (2007).
[41] A. Dumitru and Y. Nara, Numerical simulation of non-Abelian particle-field dynamics, Eur. Phys. J. A **29**, 65 (2006).
[42] B. Schenke, M. Strickland, A. Dumitru, Y. Nara, and C. Greiner, Transverse momentum diffusion and collisional jet energy loss in non-Abelian plasmas, Phys. Rev. C **79**, 034903 (2009).
[43] W. Poschl and B. Müller, Real time dynamics of colliding gauge fields and the glue burst, Phys. Rev. D **60**, 114505 (1999).
[44] W. Poschl and B. Müller, Real time evolution of soft gluon field dynamics in ultrarelativistic heavy ion collisions, arXiv:nucl-th/9903050.
[45] W. Poschl and B. Müller, Collision of SU(2) gauge fields in 3 + 1 dimensions, Comput. Phys. Commun. **125**, 282 (2000).
[46] T. Z. Esirkepov, Exact charge conservation scheme for particle-in-cell simulation with an arbitrary form factor, Comput. Phys. Commun. **135**, 144 (2001).
[47] K. Fukushima, Randomness in infinitesimal extent in the McLerran-Venugopalan model, Phys. Rev. D **77**, 074005 (2008).
[48] The code for our simulation framework is open source and publicly available at https://github.com/openpixi/openpixi.
[49] T. Lappi, Energy density of the glasma, Phys. Lett. B **643**, 11 (2006).
[50] H. Fujii and K. Itakura, Expanding color flux tubes and instabilities, Nucl. Phys. **A809**, 88 (2008).
[51] P. Romatschke and U. Romatschke, Viscosity Information from Relativistic Nuclear Collisions: How Perfect is the Fluid Observed at RHIC?, Phys. Rev. Lett. **99**, 172301 (2007).
[52] R. Ryblewski and W. Florkowski, Highly-anisotropic hydrodynamics in 3 + 1 space-time dimensions, Phys. Rev. C **85**, 064901 (2012).